Thermocline Forced by Varying Ekman Pumping. Part I: Spinup and Spindown

ZHENGYU LIU

UCAR Visiting Scientist Program, Department of Atmospheric and Oceanic Sciences, Princeton University, Princeton, New Jersey

(Manuscript received 16 January 1992, in final form 14 August 1992)

ABSTRACT

A two-layer planetary geostrophic model is used to investigate the thermocline variability under a suddenly changing Ekman pumping. The effect of ventilation and the associated advection is particularly emphasized in the ventilated zone. The governing equation is a quasi-linear equation, which is solved analytically by the method of characteristics.

It is found that the dynamics differs substantially between a shadow zone and a ventilated zone. In the shadow zone, the Rossby wave is the dominant mechanism to balance the Ekman pumping. After a sudden change in the wind field, the Ekman pumping changes rapidly, but the baroclinic Rossby wave evolves at a much slower time scale (years to decades). This mismatch of response time scale produces an imbalance in forcings and in turn results in a strong thermocline variability. However, in the ventilated zone, the cold advection replaces the Rossby wave to become the major opposing mechanism to the Ekman pumping. After a sudden wind change, both the Ekman pumping and the cold advection vary rapidly at the time scale of barotropic Rossby waves (about one week) to achieve a new steady balance, leaving little thermocline variability.

The evolution of thermocline structure and circulation differs dramatically between a spinup and a spindown. For instance, with a change in the Ekman pumping field, the lower-layer fluid in the shadow zone is no longer motionless. After a spinup, the lower-layer water moves southward because of the compression on planetary vortex tubes by the downward anomalous Ekman pumping. The associated circulation is an anticyclonic gyre. In contrast, during a spindown, the water moves northward because of the stretching of planetary vortex tubes by the upward anomalous Ekman pumping. The lower-layer circulation now consists of two counterrotating gyres: an anticyclonic gyre to the north and a cyclonic gyre to the south.

1. Introduction

Recently, our understanding of steady thermocline circulation has been substantially improved by the potential vorticity homogenization theory (Rhines and Young 1981) and the ventilated thermocline theory (Luyten et al. 1983). However, relatively little progress has been made toward understanding time-dependent thermocline circulation. On the other hand, observations show strong variability in the surface wind. For example, Levitus (1988) estimated the annual cycle of the Ekman pumping volume. The results showed that the strength of the annual Ekman pumping changes by more than 50% from its mean. Qiu and Joyce (1992) also show that at interannual time scales (about 4 yr), in the southern part of the subtropical North Pacific, the intensity of the wind stress exhibits variation of about 20% from its mean. Under such a strongly varying Ekman pumping, one naturally wonders what the response of the thermocline might be.

Observations show clear evidence of long-term change of the interior of the ocean (e.g., Roemmich and Wunsch 1984; Tabara et al. 1986; Talley and White 1987). However, little statistically significant information has been gained about the variability of large-scale thermocline structure and circulation at time scales from years to decades. Nevertheless, one thing that seems to be commonly agreed upon is that the isopycnal surfaces vary at about 5–10 m at annual time scale (below the seasonal thermocline), while they can vary at much larger amplitudes of 10 to more than 80 m for interannual time scales (4 to 10 years). In addition, most available observational works have focused on identifying baroclinic Rossby waves. Westward propagation of annual and interannual disturbances has been identified mostly in the southern parts (south of about 30°N) of the North Pacific and North Atlantic, which seems to be relevant to baroclinic Rossby waves (e.g., White and Saur 1983; Price and Magaard 1980, 1986). In contrast, in the northern parts of the North Pacific and North Atlantic, interannual baroclinic Rossby wave signals seem to be much weaker than in the southern parts. No explanation has been given to this phenomenon.

Numerical modeling of oceanic circulation has focused on the steady circulation (e.g., Cox and Bryan 1984). No systematical numerical modeling has addressed the time-dependent behavior of the thermo-

Corresponding author address: Dr. Zhengyu Liu, Program in Atmospheric and Oceanic Sciences, University of Wisconsin—Madison, 1225 West Dayton St., Madison, WI 53706.

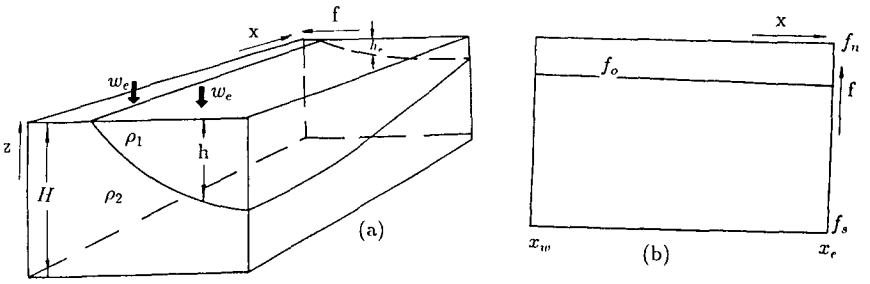

FIG. 1. Geometry of the model: (a) the three-dimensional prospective view and (b) the plan view where w_e is the Ekman pumping at the bottom of the surface Ekman layer; f_n, f_o, and f_s are, respectively, the latitude of the northern boundary of the subtropical gyre, the outcrop line, and the southern boundary of the subtropical gyre; x_e and x_w are the eastern and western boundary of the ocean; h is the interface between the two fluids with densities of ρ_1 and ρ_2; h_e is the interface depth along the eastern boundary.

cline. One difficulty facing the modelers is present poor understanding of the dynamics of the temporal behavior of the thermocline. Without clear physical insight, it is hard to explain the complicated GCM results.

So far, our understanding of the temporal behavior of the thermocline has been limited to two mechanisms: the local Ekman pumping, and the baroclinic Rossby waves that are mostly excited at the eastern boundary (e.g., Veronis and Stommel 1956; Gill and Niiler 1973; Anderson and Gill 1975). In spite of the progress already made, there are still several obvious questions to be addressed. For instance, some important aspects of Ekman pumping and Rossby waves have not been fully explored; one concern is the effects of mean flow and thermocline structure. This will be addressed in detail by Liu (1993a).

More fundamentally, besides the two mechanisms mentioned above, is there any other mechanism important for thermocline variability? One candidate is ventilation and its associated advection, which have been seen to be crucial for the theory of a steady ventilated thermocline. However, this mechanism has not been recognized for temporal variability of a thermocline. Indeed, no previous work on time-varying thermoclines has included the subduction effect. Therefore, the temporal behavior of a ventilated thermocline could not be studied. This paper, for the first time, will emphasize the ventilation effect on evolution of a thermocline. The major issues to be addressed are: How does a ventilated thermocline evolve in response to a varying wind and what are the main dynamic mechanisms behind the evolution?

To highlight the physics, this paper will examine the simplest case of varying Ekman pumping—spinup and spindown, in which the Ekman pumping suddenly increases or decreases. The case of periodic Ekman pumping will be investigated in a companion paper (Liu 1993a). This paper is arranged as follows. In section 2, we develop a two-layer planetary geostrophic model in which the evolution equation for the interface is governed by a quasi-linear equation. In section 3, in order to see the basic physics of a ventilated thermocline, we first consider a steady ventilated thermocline with emphasis on the dynamic balance for the steady thermocline. Then, we introduce temporal behavior. The solutions are obtained in two steps. First, in section 4, we manipulate the characteristic equations and reduce them into a set of algebraic equations. Then, in section 5, we derive the characteristic solutions over the entire gyre. Section 6 presents the core material of this work. The evolution of the thermocline structure and circulation will be investigated. Furthermore, the dynamics behind the evolution will be discussed in detail. It will be found that the dynamics differs dramatically between the shadow zone and the ventilated zone. As a result of the different dynamics, thermocline variability also varies significantly between the two zones. Finally, in section 7, we summarize the results and discuss some related issues.

2. The model, the equation, and its physical interpretation

a. The model and the equation

We adopt perhaps the simplest ventilated thermocline model—a two-layer, ideal fluid, planetary geostrophic model. The three-dimensional geometry of the model is displayed in Fig. 1a; ρ_1 and ρ_2 represent the densities of the upper and lower layers, respectively; h is the thickness of the upper layer, and H is the total depth. A downward Ekman pumping $w_e(x, y, t)$ is imposed at the surface. The plan view of the model is shown in Fig. 1b, where for convenience the meridional coordinate is chosen as the Coriolis parameter $f = 2\Omega \sin\theta$, with θ being the latitude. The northern and southern boundaries of a subtropical gyre where Ekman pumping vanishes are located at f_n and f_s. The lower layer outcrops at f_o. The eastern and western boundaries are set at $x_e = 0$ and $x_w < 0$.

A difference between the present model and the layered model used in classical ventilated thermocline theory (Luyten et al. 1983) is the bottom boundary.

Here, for simplicity, instead of using a motionless abyss, we employ a rigid and flat bottom,

$$H = \text{const.} \tag{2.1}$$

We should point out that for the application to the real ocean, here the bottom of the model ocean is the bottom of the main thermocline, or the depth where the directly wind-driven gyre penetrates. This imagined bottom is neither rigid nor flat. Thus, this flat bottom is artificial.

Now we derive the governing equation. For a gyre-scale circulation, the hydrostatic balance yields the dynamic pressures in both layers as

$$p_1 = \rho_0 \gamma \eta, \quad p_2 = \rho_0 \gamma (\eta - h). \tag{2.2a}$$

Here, ρ_0 is the mean density and $\gamma = g(\rho_2 - \rho_1)/\rho_0$ is the reduced gravity; η is the elevation equivalent to the upper-layer pressure such that $\gamma\eta = \rho_0(p_{\text{surface}} + g\xi)$, where ξ is the surface elevation. Implicitly, it has been assumed that $(\rho_2 - \rho_1)/\rho_0 \ll 1$. Using the planetary geostrophic approximation, the momentum equations reduce to the expressions of geostrophic balance in each layer,

$$v_n = p_{nx}/\rho_0 f, \quad u_n = -p_{ny}/\rho_0 f, \quad n = 1, 2. \tag{2.2b}$$

Furthermore, we have the Sverdrup relation and the conservation of potential vorticity $q = f/(H - h)$ south of the outcrop line (hereafter, the potential vorticity always refers to that of layer 2):

$$\beta[v_1 h + v_2(H - h)] = f w_e, \tag{2.2c}$$

$$(\partial_t + \mathbf{v}_2 \cdot \nabla) q = 0. \tag{2.2d}$$

Using (2.1) and (2.2a,b), the Sverdrup relation (2.2c) can be integrated to give

$$[2H\eta + (H - h)^2]|_0^x = 2f^2 \int_0^x w_e dx/\beta\gamma.$$

On the other hand, using (2.2a,b) and the geostrophic balance for the barotropic velocity $\mathbf{v}_B \equiv [\mathbf{v}_1 h + \mathbf{v}_2(H - h)]/H$, we have

$$\frac{1}{f\rho_0}(-p_{By}, p_{Bx}) = (u_B, v_B) = \frac{\gamma}{2fH} \times (-[2H\eta + (H - h)^2]_y, [2H\eta + (H - h)^2]_x).$$

The barotropic pressure p_B is then identified as

$$p_B = \rho_0 \gamma [2H\eta + (H - h)^2]/2H. \tag{2.3a}$$

The integrated Sverdrup relation can be rewritten in terms of p_B:

$$p_B = \rho_0 \gamma D^2/2H + p_{BE}, \tag{2.3b}$$

where

$$D^2 = 2f^2 \int_0^x w_e(x, f, t) dx/\beta\gamma; \quad p_{BE} = p_B|_{x=0} = \rho_0 \gamma [2H\eta_e + (H - h_e)^2]/2H. \tag{2.3c}$$

Here $\eta_e \equiv \eta|_{x=0}$ and $h_e \equiv h|_{x=0}$ represent, respectively, the upper-layer pressure and thickness along the eastern boundary. Equation (2.3b) states explicitly that the barotropic mode is determined instantaneously by the Ekman pumping at all times. This arises because the fast barotropic Rossby wave (with a time scale of about one week) has been filtered out by the Sverdrup relation. In other words, in our model the adjustment time for a barotropic process is infinitesimal. This assumption is reasonable because we are interested in annual and decadal time scales.

For the baroclinic mode, with (2.3a) and (2.2a,b), (2.2d) yields the evolution equation:

$$h_t + v_B h_y + [u_B + C(h)] h_x = -(1 - h/H) w_e. \tag{2.4a}$$

Here u_B, v_B, and $C(h)$ are barotropic velocity components and the speed of the nondispersive Rossby wave:

$$(u_B, v_B) = \left[-\frac{(\rho_0 \gamma D^2 + 2H p_{BE})_y}{2Hf\rho_0}, \frac{f w_e}{H\beta} \right],$$

$$C(h) = -\beta\gamma h(H - h)/f^2 H. \tag{2.4b}$$

In addition, the flat bottom (2.1) has been used. Since the barotropic flow in (2.4a) is completely determined by the Sverdrup relation (2.3b), (2.4a) is a quasilinear equation. Its characteristics are simply the group velocities of baroclinic planetary waves in the presence of a barotropic mean flow. This equation has been derived by Rhines (1986) and Dewar (1987).

Now, we nondimensionalize (2.4). For convenience, the meridional coordinate will be chosen as the Coriolis parameter f. Superscripting a dimensional quantity by a star, we have the nondimensional quantities:

$$f = \frac{f^*}{f_n}, \quad \beta = \frac{\beta^*}{\beta_0}, \quad t = \frac{t^*}{T_W}, \quad x = \frac{x^*}{L},$$

$$h = \frac{h^*}{H}, \quad \eta = \frac{\eta^*}{H}, \quad w = \frac{w^*}{W}. \tag{2.5}$$

In (2.5), W, f_n, β_0, H represent, respectively, the typical Ekman pumping velocity, the Coriolis parameter at the northern boundary of the subtropical gyre, the mean β value in a subtropical gyre, and the total depth. In addition, $T_W = H/W$, $\gamma = 2$ cm s^{-2}, $L = C_{\beta H} \times T_W$, and $C_{\beta H} = \beta_0 \times L_D^2$, $L_D^2 = \gamma H/f_n^2$ with L_D and $C_{\beta H}$ being the deformation radius and the typical midlatitude Rossby wave speed. Then T_W is the advective time scale for a particle to sink to the bottom of the main thermocline, and L is the zonal scale across which a midlatitude planetary wave travels in one advective time scale. If we choose the parameters as $W = 10^{-4}$ cm s^{-1}, $f_n = 2\Omega \sin(45°) = 10^{-4}$ s^{-1}, $H = 600$ m, $\beta_0 = (2\Omega/a)\cos(35°) = 1.87 \times 10^{-13}$ s^{-1} cm^{-1}, it follows that $T_W \approx 20$ yr, $L \approx 8400$ km, $C_{\beta H} \approx 1.6$ cm s^{-1}, and $L_D \approx 33$ km. With (2.5), (2.4a) becomes

$$h_t + \mathbf{v}_B \cdot \nabla h + C(h) h_x = -(1 - h) w_e, \tag{2.6a}$$

where (2.4b) and (2.3c) give

$$u_B = -\frac{1}{2f}[D^2 + p_{BE}]_f,$$

$$v_B\left(\equiv \frac{df}{dt}\right) = fw_e,$$

$$C(h) = -h(1-h)/f^2,$$

$$D^2 = 2f^2 \int_0^x w_e dx. \qquad (2.6b)$$

For simplicity, in (2.6) we have chosen an exact β plane such that $f = f_m + \beta_0 y$, where f_m is the mean latitude of a subtropical gyre. The nondimensional β has been assigned a value of unity.

b. Physical interpretation of the evolution equation

The physics behind (2.6a) [or (2.4a)] can be made clear as follows. First, we rewrite (2.4a) as

$$h_t = -\mathbf{v}_B \cdot \nabla h - Ch_x - (1 - h/H)w_e(f). \quad (2.7)$$

The terms on the right-hand side will be called, in order, the density advection, the Rossby wave, and the effective local Ekman pumping. The corresponding energy equation is

$$P_t = -\mathbf{v}_B \cdot \nabla P - CP_x - (1 - h/H)hw_e(f),$$

where $P = h^2/2$ is the available potential energy, $-\mathbf{v}_B \cdot \nabla P$ is the energy advection by the barotropic flow, $-CP_x$ is the energy radiated by Rossby waves, and $-(1 - h/H)hw_e(f)$ is the rate of work done by the effective local Ekman pumping. The dynamic effects of the three mechanisms are illustrated below.

The effective local Ekman pumping $-(1 - h/H)w_e(f)$, roughly speaking, consists of two parts: the surface Ekman pumping $-w_e$ and the divergent Ekman pumping mass flux in the upper layer $-(h/H)w_e = h\nabla \cdot \mathbf{v}_B$. Since the latter part of mass input diverges in the upper layer before it reaches the interface, it will not affect the evolution of the interface. As a result, the fraction of the surface Ekman pumping able to influence the interface is the remaining part $-w_e - (-hw_e/H) = -(1 - h/H)w_e(f)$. This effective Ekman pumping is still downward but weaker than the surface Ekman pumping. The response is a deepening of the interface $h_t > 0$ as stated in (2.7). From the energy viewpoint, the local Ekman pumping is an external energy source that forces lighter fluid to descend. Hereafter, without confusion, the effective local Ekman pumping is simply called Ekman pumping.

The Rossby wave mechanism $-Ch_x$ is caused by the westward propagation of a planetary wave. In a subtropical gyre, an isopycnal usually deepens westward, that is, $h_x < 0$ on the gyre scale. Thus, the westward propagation of a Rossby wave produces a local ascent of the interface, that is, $h_t < 0$ as observed from (2.7). In other words, a Rossby wave locally transports available potential energy westward.

The term $-\mathbf{v}_B \cdot \nabla h$ is called the density advection because in a two-layer model, the advection of the interface h is the analogy of a density advection. Here, a dense fluid advection (cold advection) $-\mathbf{v}_B \cdot \nabla h < 0$ is simulated by an excess lower-layer fluid advection. This advection locally produces a thicker lower layer ($h_t < 0$), which implies a local reduction of heat storage or energy. The opposite occurs for a light fluid advection (warm advection).

Hence, the Ekman pumping provides the driving force for the thermocline circulation. To achieve a steady state, either a Rossby wave or a cold advection is required to balance this force. This will be seen clearly in the next section. Finally, it is interesting to see a relation between the density advection and the β spiral, which is a measure of the vertical velocity shear. In light of (2.2a,b) and (2.4c), one obtains

$$\mathbf{k} \cdot (\mathbf{v}_1 \times \mathbf{v}_2) = \mathbf{v}_B \cdot \nabla h. \qquad (2.8)$$

This relation means that a β-spiral structure [$\mathbf{k} \cdot (\mathbf{v}_1 \times \mathbf{v}_2) < 0$] corresponds to cold advection while an anti-β spiral structure [$\mathbf{k} \cdot (\mathbf{v}_1 \times \mathbf{v}_2) > 0$] gives warm advection. This relation between density advection and vertical shear can be easily proven in a continuously stratified model even in the presence of temporal variations. Therefore, the observed β spiral in the interior mean thermocline in the subtropical gyre (Stommel and Schott 1977) implies a mean southward cold advection there, consistent with our intuition.

3. The dynamics of a steady ventilated thermocline

Before we analyze a time-dependent thermocline, it is helpful to discuss briefly a steady ventilated thermocline in our two-layer model. For simplicity, we only consider the case in which both the Ekman pumping w_e and outcrop line f_o are zonal. In addition, as in the classical LPS model (Luyten et al. 1983), we assume that there is no mass flux into the eastern boundary in each layer, that is, $p_{1f}|_{x=0} = p_{2f}|_{x=0} = 0$, which, by virtue of (2.2a), is equivalent to $\eta_e = \text{const}$, $h_e = h_e(f_o) = 0$. Thus,

$$w_e = w_1(f), \quad f_o = \text{const}, \quad \eta_e = \text{const}, \quad h_e = 0. \qquad (3.1)$$

Following Luyten et al. (1983), we derive the solution. In the ventilated zone, the steady form of potential vorticity conservation (2.2d) and the geostrophic balance (2.2b) give $f/(1 - h) = Q(p_2)$. Along the outcrop line, this becomes $Q(p_2) = f_o = \text{const}$. Thus, we have the solution for the ventilated zone as

$$f/(1 - h) = f_o = \text{const}, \quad \text{or} \quad h = 1 - f/f_o. \quad (3.2)$$

In the shadow zone, $\mathbf{v}_2 = 0$. With the aid of (2.2a,b), this means $p_2 = \eta - h = \text{const}$. Using the nondimen-

sional form of the Sverdrup relation (2.3b), we have the shadow zone solution:

$$h^2 = 2f^2 w_1 x. \tag{3.3}$$

The shadow zone boundary will be denoted by B_1. The continuity of the solution (3.2) and (3.3) along B_1 gives the expression for B_1 as

$$x_{B1}(f) = (1 - f/f_o)^2/2f^2 w_1(f). \tag{3.4}$$

Now, we analyze the dynamic balance for the steady solution (3.2) and (3.3). In the steady case, Eq. (2.6a) degenerates to

$$\mathbf{v}_B \cdot \nabla h + Ch_x = -(1 - h)w_e. \tag{3.5}$$

In the ventilated zone, the solution (3.2) has no zonal slope $h_x = 0$. Thus, in the ventilated zone, the Rossby wave term vanishes $Ch_x = 0$ and the dynamic balance is achieved between the cold advection energy sink and the Ekman pumping energy source; that is,

$$\mathbf{v}_B \cdot \nabla h = -(1 - h)w_e > 0. \tag{3.6}$$

Rossby waves play no role in the dynamic balance in the ventilated zone here. The cold advection in (3.6) also means a β-spiral velocity shear in the ventilated zone as indicated by (2.2).

In contrast, in the shadow zone, $\mathbf{v}_2 = 0$ and (2.8) yield $-\mathbf{v}_B \cdot \nabla h = 0$. Therefore, the dynamic balance is such that all the energy input from the Ekman pumping is transported westward by planetary waves; that is,

$$Ch_x = -(1 - h)w_e > 0. \tag{3.7}$$

This simple example illustrates the intrinsic dynamic difference between a ventilated zone and a shadow zone. The Ekman pumping is important for both regions as the driving mechanism. However, in balancing this driving, the ventilated zone is dominated by density advection while the shadow zone is controlled by planetary waves. Intuitively, this difference of dynamics between the two zones is sensible. In a ventilated zone, the subduction of waters play a crucial role. Thus, advection is important. In a shadow zone, however, there is no motion except in the surface layer. Thus, advection is not crucial.

As far as time variability is concerned, the dynamic balances (3.6) and (3.7) have completely different natures and may result in totally different variability. For instance, we consider the case in which the wind stress suddenly changes. Let us tentatively analyze the dynamical balance in the two zones. In the ventilated zone, both the Ekman pumping $-(1 - h)w_e$ and the density advection $\mathbf{v}_B \cdot \nabla h$ vary rapidly at the barotropic Rossby time scale. Therefore, a new steady dynamical balance (3.6) may be rapidly achieved. This may imply little variability of the interface. In the shadow zone, the situation is totally different. The baroclinic Rossby wave $C(h)h_x$ varies only after a slow baroclinic Rossby wave time scale, while the Ekman pumping has been changed rapidly right after the change of the wind stress. Therefore, the steady balance (3.7) cannot be maintained. An imbalance in the steady dynamic balance is produced. This requires strong temporal variability of the interface. Consequently, responding to this changing wind, there is little variability in the ventilated zone, but there is a strong variability in the shadow zone. Later in section 6, it will be proven that this is indeed the case.

Finally, one notices that the ventilated zone solution (3.2) is peculiar because of its uniform potential vorticity $f/(1 - h) = f_o = \text{const}$. This uniform potential vorticity is an artificial feature of our model. Indeed, it is the flat bottom, together with a zonal outcrop line, that produces a constant subduction potential vorticity f_o along the outcrop line and, in turn, the uniform potential vorticity in the whole ventilated zone. The absence of Rossby waves is caused by this uniform potential vorticity because there is no background potential vorticity gradient to provide the restoring mechanism. If the outcrop line varies with latitude, the potential vorticity along the outcrop line will not be uniform. Thus, the potential vorticity in the lower layer will not be uniform and Rossby waves will appear in the ventilated zone. In reality, the potential vorticity in a ventilated zone is definitely not uniform. However, observations (e.g., Keffer 1985; Talley 1988), numerical models (Cox and Bryan 1984; Cox 1985, 1987), and theories with more complex models (e.g., Luyten et al. 1983; Pedlosky and Young 1983; Liu et al. 1993) all find that the potential vorticity in a ventilated zone, although not uniform, is much more uniform than that in a shadow zone. This suggests much weaker planetary wave activity in a ventilated zone than in a shadow zone. Hence, the different natures of dynamical balances will still exist. [For a more detailed discussion, the reader should refer to section 6 of chapter 2 of Liu (1991).]

4. Characteristic equations

Now, we return to the time-dependent evolution. We solve (2.6a) by the method of characteristics. First, we manipulate the characteristic equations and simplify them. The characteristic equations for (2.6a) are given by

$$\frac{dt}{ds} = 1, \tag{4.1a}$$

$$\frac{df}{ds} = fw_e(x, f, t), \tag{4.1b}$$

$$\frac{dh}{ds} = -(1 - h)w_e(x, f, t), \tag{4.1c}$$

$$\frac{dx}{ds} = -\frac{1}{2f}[D^2(x, f, t) + p_{BE}(f, t)]_f - h(1 - h)/f^2, \tag{4.1d}$$

where s is the variable along a characteristic. The initial condition for characteristics in (4.1) is

$$(t, f, x, h)|_{s=0} = [t_i, f_i, x_i, h_i(x_i, f_i, t_i)]. \quad (4.2)$$

This is different from the real-time initial condition at $t = 0$, with $h(x, f, t)|_{t=0}$. Equation (4.1) is a set of ordinary differential equations. A simple case occurs when the Ekman pumping is independent of longitude; that is, $w_e = w_e(f, t)$. In this case, (4.1) can be solved one by one: (4.1a) for t, (4.1b) for f, (4.1c) for h, and finally (4.1d) for x.

Hereafter, for simplicity, we adopt an eastern boundary condition of no barotropic zonal transport into the eastern boundary (Pedlosky 1983). Hence, it follows that

$$u_B|_{x=0} = -\partial_f p_{BE}/f = 0. \quad (4.3)$$

The simplest interface structure to satisfy this eastern boundary condition is $h_e = 0$ [see (3.1)], as is the case in Luyten et al. (1983). However, the eastern boundary condition (4.3) allows any $h_e(f, t)$ once the corresponding $\eta_e(f, t)$ makes p_{BE} in (2.6b) spatially constant.

For a spinup or spindown process, we assume the Ekman pumping suddenly changes from an old w_1 to a new w_2 at a time $t = 0$; that is,

$$w_e(f, t) = \begin{cases} w_1(f), & t < 0 \\ w_2(f), & t \geq 0. \end{cases} \quad (4.4)$$

With (4.4), we can integrate (4.1a,b) to yield

$$t = t_i + s, \quad t \leq 0 \quad (4.5a)$$

$$s = \int_{f_i}^{f} d\mu/\mu w_2(\mu) \quad \text{or } \textit{implicitly} \quad f = \hat{f}(f_i, s). \quad (4.5b)$$

In addition, (for a general Ekman pumping) the division of (4.1b) and (4.1c) recovers the conservation of potential vorticity (2.2d) along a characteristic:

$$\frac{d}{ds}\left(\frac{f}{1-h}\right) = 0, \quad \text{or} \quad \frac{f}{1-h} = \frac{f_i}{1-h_i}. \quad (4.5c)$$

This can be used to replace (4.1c). Finally, the differential form of (4.5b) is $ds = df/fw_2(f)$. This allows us to use f to replace s as the characteristic variable. Substituting this into (4.1d) and noting (4.3) and (4.5c), the x equation (4.1d) can be put in the form

$$\frac{d}{df}[f^2 w_2(f)x] = -\frac{1-h_i}{f_i}h = -\frac{1-h_i}{f_i}\left[1-(1-h_i)\frac{f}{f_i}\right].$$

This can be integrated to give

$$2f^2 w_2(f)x = 2f_i^2 w_2(f_i)x_i + h^2 - h_i^2. \quad (4.5d)$$

In addition, sometimes it will be found convenient to be able to replace (4.5b) by the inverse function $\hat{f}_i$,

$$f_i = \hat{f}_i(f, s), \quad (4.5e)$$

which satisfies $f \equiv \hat{f}[\hat{f}_i(f, s), s]$. For illustration, we present two examples of the $\hat{f}$ characteristic solution. The first is a spatially uniform Ekman pumping

$$w_e(f) = W_0, \quad (4.6a)$$

where $W_0 < 0$ is a constant. Equations (4.5b,e) then yield the $\hat{f}$ and $\hat{f}_i$ as

$$\hat{f} = f_i e^{W_0 s} \quad \text{and} \quad \hat{f}_i = fe^{-W_0 s}. \quad (4.6b)$$

The second is a parabolic Ekman pumping

$$w_e(f) = W_0(1-f)(f-f_s), \text{ where } f_n = 1. \quad (4.7a)$$

This will be adopted to study an entire subtropical gyre for the spinup problem. Its $\hat{f}$ function is implicitly determined by

$$\frac{1-f_s/\hat{f}}{(1/\hat{f}-1)^{f_s}} = \frac{1-f_s/f_i}{(1/f_i-1)^{f_s}}\exp[f_s(1-f_s)W_0 s]. \quad (4.7b)$$

Equations (4.5a–d) are essentially a set of algebraic equations. When the initial condition (4.2) is specified, (4.5) can be solved. After solving for h from this set of equations, the nondimensional pressures can be readily obtained from the nondimensional form of (2.1a) and the Sverdrup relation (2.3c) as $p_1 = \eta$ and $p_2 = \eta - h$. Then, the velocities can be determined by the nondimensional form of (2.2b) as $(u_n, v_n) = (-p_{nf}, p_{nx})/f$ for $n = 1, 2$.

5. Characteristic solutions

With the characteristic equations in (4.5), solutions at different times can be derived for the entire gyre. Suppose we want to derive the solution at the time $t = T$. The solution will be formed by characteristics starting from the eastern boundary, the outcrop line, and the initial time $t = 0$ plane. Different zones will be determined by characteristics coming from different starting points. We start with the part of the solution established by the characteristics originating from the eastern boundary.

a. The new shadow zone

For that part of the solution due to characteristics from the eastern boundary, each characteristic curve must start at a time t_i before T on the eastern boundary, that is, $0 < t_i < T$, $x_i = x_e = 0$. In the (t_i, x_i, f_i) space, one example characteristic line is shown schematically in Fig. 2a with the thick, dark arrow. This characteristic curve starts from the surface $0 < t_i < T$, $x_i = x_e$ and ends on the plane $t_i = T$. For simplicity, the interface depth at the eastern boundary is chosen to be

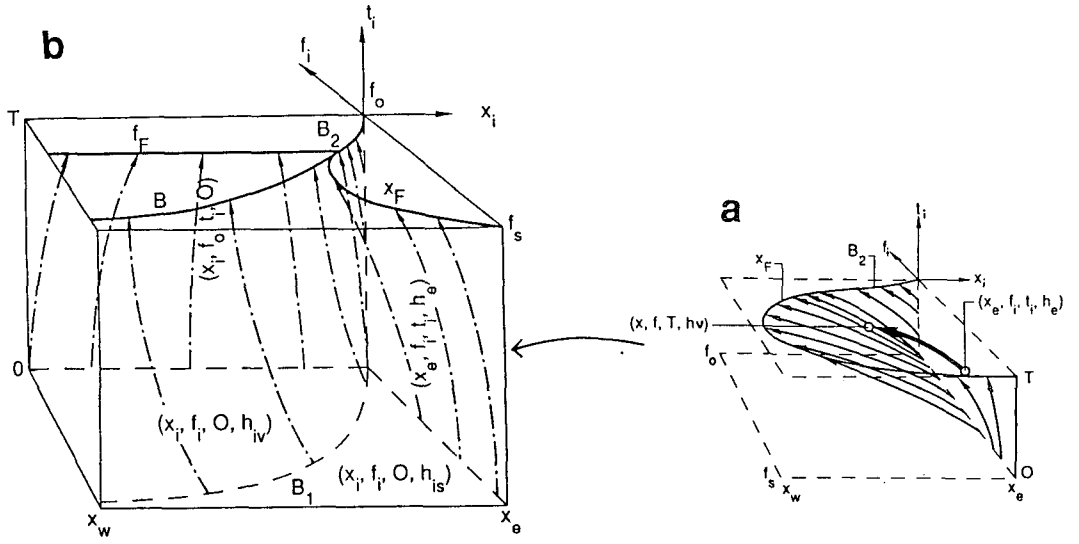

FIG. 2. Schematic figures for characteristics and the wave fronts in the three-dimensional characteristic space. Panel (a) shows how the new shadow zone develops from the change in Ekman pumping at $t = 0$ until some later time $t = T$. The dashed lines are the outcrop line (at $f = f_0$), the eastern boundary $x = x_e$, and the westernmost edge $x = x_w$ of the calculation. The thick, dark arrow represents a typical characteristic originating from the eastern boundary at some time after the change in Ekman pumping; such characteristics determine the steady solution in the new shadow zone. The thin arrows show two groups of characteristics: the first group started from the eastern boundary at $t = 0$ and later set the solution along the part x_F of the boundary between old and new shadow zones; the second group left the corner (x_e, f_0) at later times and set the solution along the part B_2 of the boundary between the new shadow zone and the new ventilated zone. (b) The wave fronts and the associated characteristics in the (t_i, x_i, f_i) characteristic space. Four groups of characteristics are drawn. The first group started from the eastern boundary x_e at the initial time 0, forming the eastern boundary wave front x_F, which separates the new shadow zone and the original shadow zone. The new shadow zone is established by characteristics from the eastern boundary at later times, while the original shadow zone by characteristics from the shadow zone at initial time 0 (i.e., the initial shadow zone h_{is}). The second group started from the outcrop line f_o at the initial time 0, establishing the advection front f_F, which separates the new ventilated zone from the original ventilated zone. The new ventilated zone is built by characteristics originating from the outcrop line at later times, while original ventilated zone is built by characteristics from the ventilated zone at initial time 0 (i.e., the initial ventilated zone h_{iv}). The third group started from the corner (x_e, f_o) at later times $0 < t < T$, forming the part of the new shadow zone boundary B_2, which separates the new ventilated zone and the new shadow zone. The last group started from the old shadow zone boundary B_1 at the initial time 0, evolving into the internal front B, which separates the original ventilated from the original shadow zone.

$h|_{x=0} = 0$. The initial condition for the characteristics becomes

$$x_i = 0, \quad h_i = 0, \quad 0 < t_i < T, \quad f_s < f_i < f_o. \tag{5.1}$$

The characteristic solution (denoted by h_s) established by (5.1) is obtained from (4.5a–d) as

$$t = t_i + s, \quad 0 \leqslant s \leqslant T - t_i, \tag{5.2a}$$

$$f = \hat{f}(f_i, s), \tag{5.2b}$$

$$h_s = 1 - f/f_i, \tag{5.2c}$$

$$2f^2 w_2(f) x = h_s^2. \tag{5.2d}$$

Equation (5.2d) immediately gives an explicit solution $h_s = \sqrt{2f^2 w_2(f) x}$. This is the same as the steady shadow zone solution in (3.3) except for the new Ekman pumping w_2. Therefore, solution (5.2) is called the new shadow zone solution.

However, different from the steady case in (3.3), at a finite time, the solution (5.2) is valid only behind (to the east of) the earliest wave front, established by the characteristics at the start time $t = 0$. This wave front will be denoted by x_F and is shown schematically in Fig. 2a. In the figure, the characteristics (thin arrowed curves) forming x_F start from the line $t_i = 0$ and $x_i = 0$, and end on x_F at $t_i = T$. To show the wave front and the associated characteristics more clearly, Fig. 2b is plotted showing the wave front x_F (other wave fronts will be discussed later) and the associated characteristics in the whole (t_i, x_i, f_i) space (for $0 < t_i < T$). (The characteristic space in Fig. 2a is a part of the space in Fig. 2b near the eastern boundary.) The initial condition of x_F is derived by substituting $t_i = 0$ into (5.1). Therefore, x_F is obtained in (5.2) by letting $t_i = 0$:

$$x_F(f, t) = [1 - f/\hat{f}_i(f, t)]^2 / 2f^2 w_2(f), \tag{5.3}$$

where the inverse $\hat{f}_i$ function in (4.5e) has been used. This is a planetary wave front in the presence of a Sverdrup flow. It propagates westward at the characteristic

speed $dx/dt = u_B + C(h)$. As time passes, x_F propagates, behind which the new shadow zone is expanded. The expansion can be seen in Fig. 2a or 2b on succeeding t_i planes. More clearly, the evolution is seen in the top view in Fig. 3. At the initial time $t = 0$ (Fig. 3a), x_F has not propagated yet. There is no new shadow zone. The gyre is filled with the initial steady ventilated thermocline [h_{iv} as in (3.2) and h_{is} as in (3.3)]. Later (in Fig. 3b), x_F advances westward, and near the eastern boundary a new shadow zone is established. Even later (in Fig. 3c), x_F reaches farther west and the new shadow zone is greatly expanded.

In addition, similar to the steady case of (3.4), to the north of the new shadow zone, there is a new shadow zone boundary B_2. This B_2 is formed by the characteristics (also shown as thin arrows in Fig. 2a,b) starting from the line $x_i = 0, f_i = f_o$, and $0 < t_i < T$. The equation for B_2 can be obtained from (5.2) and will be seen the same as the old shadow zone boundary B_1 in (3.4) except for a new Ekman pumping w_2.

b. *The new ventilated zone*

Similar to the new shadow zone, there is another group of characteristics originating from the outcrop line f_o at $0 < t_i < T$ (the figure similar to Fig. 2a is not presented). If we use a zonal outcrop line f_o = const, the initial surface for characteristics is

$$f_i = f_o, \quad h_i = 0, \quad 0 < t_i < T, \quad x_w < x_i < 0. \tag{5.4}$$

The solution (h_v) is derived by substituting (5.4) into (4.5a–d) as

$$t = t_i + s, \quad 0 \leqslant s \leqslant T - t_i, \tag{5.5a}$$

$$f = \hat{f}(f_o, s), \tag{5.5b}$$

$$h_v = 1 - f/f_o, \tag{5.5c}$$

$$2f^2 w_2(f)x = 2f_o^2 w_2(f_o)x_i + h_v^2. \tag{5.5d}$$

Equation (5.5c) is already an explicit solution, which is the same as the steady ventilated zone in (3.2) with the new boundary B_2 in (5.4) on the eastern flank. Therefore, solution (5.5) is called the new ventilated zone solution.

In the time-varying case, similar to the new shadow zone discussed above, the new ventilated zone is established after the passing of the earliest wave front f_F, which starts from the outcrop line f_o at the beginning $t_i = 0$ and advances southward; f_F is then formed by the part of characteristics in (5.4b) with $t_i = 0$ (the line with $t_i = 0, f_i = f_o$ in Fig. 2b). These characteristics and f_F are also shown in Fig. 2b. Substituting $t_i = 0$ into (5.5b), this wave front can be derived,

$$f_F(t) = \hat{f}(f_o, t). \tag{5.6}$$

For instance, a uniform Ekman pumping in (4.6) has $f_F(t) = f_o e^{W_0 t}$. In general, f_F advances southward at the characteristic speed (in our model, this is also the Sverdrup velocity) $df/dt = v_B = fw_2$. As time passes, f_F travels farther south, and thus the new ventilated zone is expanded. The expansion can be seen in Fig. 3 at succeeding times.

The newly formed ventilated zone (h_v) and shadow zone (h_s) are due to information coming from the boundaries of the gyre. Therefore, they are boundary value solutions for the partial differential equation

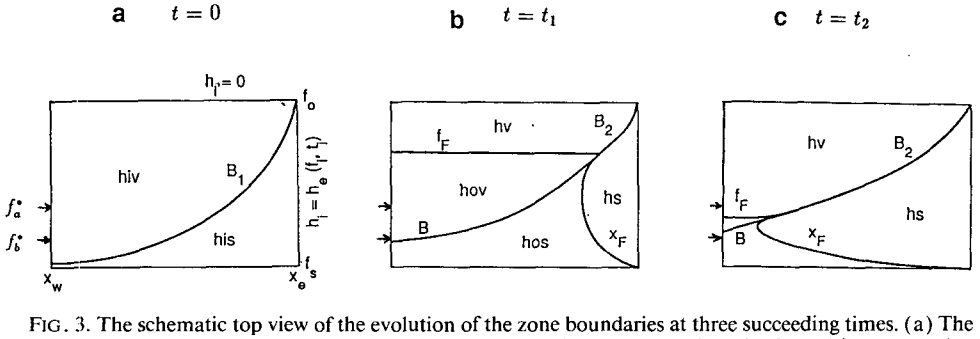

FIG. 3. The schematic top view of the evolution of the zone boundaries at three succeeding times. (a) The initial time $t = 0$. The gyre is occupied by the initial steady ventilated thermocline with h_{iv} and h_{is} representing the initial ventilated zone and shadow zone, respectively (see Fig. 2b at $t_i = 0$). The initial h value for the new ventilated zone is $h_i = 0$ because on the outcrop line the initial h value for the new shadow zone is the eastern boundary isopycnal value h_e. The advection wave front f_F and eastern boundary wave front x_F stay at their initial positions on the outcrop line f_0 and the eastern boundary x_e, respectively. (b) At a later time t_1 when wave fronts x_F and f_F have advanced westward and southward, respectively, establishing a new shadow zone near the eastern boundary and a new shadow zone near the outcrop line. The original ventilated zone and shadow zone starting from the initial ventilated zone and shadow zone h_{iv} and h_{is} in (a) have shrunk. (c) At an even later time t_2, when the new ventilated zone and the new shadow zone have occupied almost all the basin except in the southwestern corner. A new ventilated thermocline is established over almost the entire basin. Note that f_a^* and f_b^* indicate the latitudes of sections in Figs. 4a and 4b, respectively. The difference between the two is that at time t_2, f_F has passed f_a^*, therefore establishing a new steady state on this latitude; but has not reached f_b^*, leaving a still varying zonal section (see Fig. 4).

(2.6a). The Ekman pumping (4.4) is steady after the initial time. The boundary conditions h_e or f_o are also steady [in (5.1) and (5.4)]. Thus, the solutions (5.2) and (5.5) are steady.

c. The original ventilated zone and original shadow zone

From Fig. 3, we see that, at each time, before the arrival of the wave front f_F and x_F, the gyre is occupied by some other solution. This solution is due to the real-time initial value (at $t = 0$) and is formed by the characteristics starting from the plane with $t_i = 0$ and within the gyre $x_w < x_i < x_e, f_s < f_i < f_o$ (the figure similar to Fig. 2a is not presented). Thus, the initial surface for the characteristics is

$$t_i = 0, \quad h_i = h_i(x_i, f_i), \qquad x_w < x_i < 0, \quad f_s < f_i < f_o. \tag{5.7}$$

Furthermore, initially at time $t = 0$, there are two different zones in the gyre (see Fig. 3a): the old ventilated zone in (3.2) and the old shadow zone in (3.3), which are denoted, respectively, by

$$h_i = h_{iv}(x_i, f_i) = 1 - f_i/f_o \quad \text{for} \quad x_i < x_{B1}(f_i), \tag{5.8}$$

and

$$h_i = h_{is}(x_i, f_i) = f_i\sqrt{2w_1(f_i)x_i} \quad \text{for} \quad x_i > x_{B1}(f_i). \tag{5.9}$$

The solution obtained from (5.7), (5.8), and (4.5a–d) will be named the original ventilated zone (h_{ov}),

$$t = s, \quad 0 \leqslant s < T, \tag{5.10a}$$

$$f = \hat{f}(f_i, s), \tag{5.10b}$$

$$h_{ov} = 1 - [1 - h_{iv}(x_i, f_i)]f/f_i, \tag{5.10c}$$

$$2f^2w_2(f)x = 2f_i^2 w_2(f_i)x_i + h_{ov}^2 - h_{iv}^2. \tag{5.10d}$$

The solution derived from (5.7), (5.9), and (4.8) will be called the original shadow zone (h_{os}),

$$t = s, \quad 0 \leqslant s \leqslant T \tag{5.11a}$$

$$f = \hat{f}(f_i, s), \tag{5.11b}$$

$$h_{os} = 1 - [1 - h_{is}(x_i, f_i)]f/f_i, \tag{5.11c}$$

$$2f^2w_2(f)x = 2f_i^2 w_2(f_i)x_i + h_{os}^2 - h_{is}^2. \tag{5.11d}$$

The boundary between h_{ov} and h_{os}, denoted by B, is initially at the old shadow zone boundary $x = x_{B1}(f)$ in (3.4). Later, B evolves with time. With the initial condition $x_i = x_{B1}(f_i)$, B can be derived from (5.10) or (5.11) as $x = x_B(f, t)$ (not presented here). It forms an internal wave front starting at B_1. As shown schematically in Fig. 3, initially, the h_{ov} (or h_{iv} at $t = 0$) and h_{os} (or h_{is} at $t = 0$) occupy the whole gyre. Later, x_F propagates westward and f_F advances southward, the new shadow zone and the new ventilated zone are expanded. At the same time, the original ventilated zone and the original shadow zone shrink. At the last time shown in Fig. 3c, the new shadow zone and the new ventilated zone occupy almost all of the gyre except for the southwestern corner. Eventually, the new shadow zone and ventilated zone will overtake the entire gyre, establishing a new ventilated thermocline.

6. Spinup and spindown of a ventilated thermocline

a. The solutions

Now, we present the core material of the paper—the spinup and spindown of a ventilated thermocline. For clarity, we first derive explicit solutions in (t, x, f) coordinate by virtue of the parametric solutions (in the characteristic coordinate) obtained in the last section. The solution for the new shadow zone is easily derived from (5.2d) as

$$h_s^2 = 2f^2w_2(f)x. \tag{6.1}$$

This part of the solution is established after the passing of the earliest eastern boundary wave front x_F and is bounded to the northwest by the new shadow zone boundary B_2. The new ventilated zone solution is obtained from (5.5c) directly as

$$h_v = 1 - f/f_o. \tag{6.2}$$

This solution is bounded to its east by the new shadow zone boundary B_2 and is established after the earliest outcrop line wave front f_F in (5.6). The thermocline in the new shadow zone (6.1) and ventilated zone (6.2) are steady. Eventually, we expect (6.1) and (6.2) should become established all over the gyre and to form a new steady ventilated thermocline under w_2.

However, at a finite time, in the region where x_F and f_F have not arrived, the thermocline is undergoing transient adjustment. The solutions in these regions are the original ventilated zone and shadow zone, given, respectively, by (5.10) and (5.11). Substituting the initial condition (5.8) into h_{ov} in (5.10) yields the explicit solution

$$h_{ov} = 1 - f/f_o. \tag{6.3}$$

This solution is bounded to the north by f_F and to the east by the internal wave front B in (5.13). Surprisingly, (6.3) shows that h_{ov} is independent of time. In fact, the structure of h_{ov} is exactly the same as the initial ventilated zone h_{iv} in (5.8) and the new ventilated zone (6.2). This peculiar feature is due to the flat bottom and the zonal outcrop line, which produce a uniform potential vorticity in the ventilated zone [$q = f/(1 - h) = q|_{f=f_o} = f_o = \text{const}$].

Finally, the solution for the original shadow zone (h_{os}) is derived by substituting $h_{is} = 1 - (1 - h_{os})f_i/f$ and $x_i = h_{is}^2/[2f_i^2 w_1(f_i)]$ [from (5.11c) and (5.9)]

into (5.11d) to yield a quadratic equation for h_{os} and x, whose standard form can be written as

$$G \times (x - x_0) = (h_{os} - h_0)^2, \qquad (6.4a)$$

where

$$G = \frac{2I^2 f^2 w_2(f)}{\delta(I^2 - \delta)}, \quad h_0 = \frac{(I-1)\delta}{I^2 - \delta},$$

$$x_0 = \frac{-(I-1)^2\delta}{2f^2 w_2(f)(I^2 - \delta)}, \qquad (6.4b)$$

$$\delta(f, t) \equiv \delta(\hat{f}_i) = 1 - w_2(\hat{f}_i)/w_1(\hat{f}_i),$$

$$I(f, t) \equiv f/\hat{f}_i \leqslant 1, \qquad (6.4c)$$

and h_{os} is bounded to the west by the eastern boundary wave front x_F and to the east by the internal wave front B; that is,

$$x_B(f, t) \leqslant x \leqslant x_F(f, t). \qquad (6.4d)$$

Equations (6.4a–c) give a parabolic zonal profile with G as the curvature and (x_0, h_0) as the nose. The physical part of the solution h_{os} is only the section between x_B and x_F as indicated in (6.4d). Equations (6.1)–(6.4) give the explicit solution over the entire gyre.

b. *Thermocline evolution*

We first consider the evolution of a zonal profile. Along a given latitude f, before the arrival of f_F, a zonal profile consists of three parts (refer to Fig. 3b,c): a flat and unchanging h_{ov} of (6.3) to the west of B, a steady parabolic h_s in (6.1) to the east of x_F, and a changing parabolic h_{os} of (6.4) in the middle. When f_F reaches this latitude at time t_F satisfying

$$f_F[t_F(f)] \equiv f, \qquad (6.5)$$

where f_F is given in (5.6), B and x_F merge. Therefore, the width of the transient middle part of h_{os} diminishes. At the same time, the western side is replaced by the new ventilated zone (6.2). Later, a steady circulation is established on this latitude with the varying B replaced by the new steady B_2. Schematic figures for a spinup and a spindown process are given in Fig. 4a and Fig. 4b, respectively.

Since h_{os} is the only part whose structure varies with time, a detailed discussed of its evolution is useful and is given in the Appendix. Here, we only describe the result briefly. After a spinup, the interface simply keeps deepening in the h_{os} part until it reaches the local depth of the new steady shadow zone or ventilated zone. On a latitude f, this transient process continues until the arrival of front f_F at time $t = t_F$ (see Fig. 4a). The spindown process is more complex. The interface shallows before it reaches the depth of the new steady shadow zone (profiles in Fig. 4b before t_b). Moreover, the interface may become gravitationally unstable as shown by the $t = t_b$ profile in Fig. 4b. This implies breaking of planetary waves, which is caused by the steepening of nonlinear planetary wave $C(h) \sim h(1 - h)$ (Anderson and Killworth 1979; Dewar 1987). Therefore, in principle, the evolution during a spindown differs significantly from that of a spinup in which breaking never occurs. Nevertheless, it should be pointed out that the breaking for a spindown will not occur in a model ocean with a realistic width. This occurs because the very gentle slope of the thermocline takes too long a time ($t > O(1)$) for the nonlinear

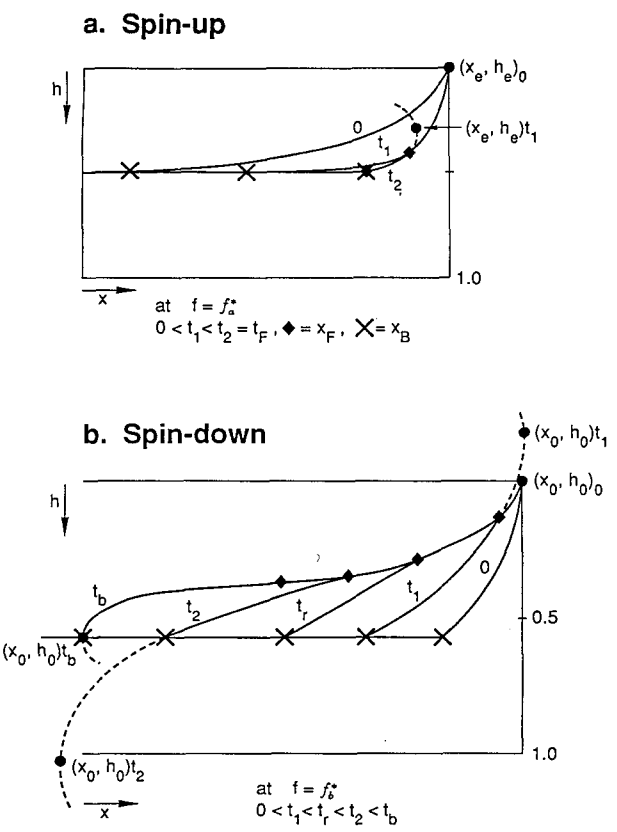

FIG. 4. Schematic figures for the evolution of zonal profiles and the positions of the eastern boundary wave front x_F (black diamond), the internal front x_B (black cross), and the nose of the parabola (black dot) of the isopycnal on the section. The dashed lines are the parabola, which does not belong to the physical solution; they are drawn only to delineate the nose of the parabola. The figure is explained in detail in the Appendix. Panel (a) shows three succeeding times of a zonal profile in the spinup case. The corresponding latitude f_a^* is indicated in Fig. 3. The isopycnal starts from initial time 0, and deepens to the profile at t_1, and then deepens further. Later at t_2 the advection front f_F has passed this section, establishing a new steady state with a ventilated zone on the right and a new shadow zone on the left. Here, t_F is the time for f_o to arrive at this latitude as defined in (6.5). Panel (b) depicts five sections in a spindown case. The latitude is at f_b^*, which is indicated schematically in Fig. 3. The profile starts from the initial shadow zone section at $t = 0$; it shallows over time. Before t_r, the nose of the parabola bulges downward as in the initial time; after t_r, the nose starts to bulge upward. Before t_b, the nose is not of the solution. At time t_b, the nose first becomes a part of the solution. This is the time of breaking because of gravitational instability. Here, we have assumed that the breaking occurs before the arrival of f_o, that is, $t_b < t_F$ [see (A.3) for t_b].

steepening to function. By that time, the Rossby wave has propagated far away from the western boundary, and therefore the breaking occurs well beyond the western boundary. One may think that the breaking may occur if the perturbation is very localized. We speculate that this is the case. Indeed, some examples of breaking due to planetary waves forced at the eastern boundary are given in Liu (1992c).

c. *Circulation evolution*

Now, we analyze the two-dimensional structure of the thermocline and circulation with emphasis on the lower-layer circulation. Figure 5 and Fig. 6 show two cases with a parabolic Ekman pumping in (4.7). Figure 5 displays the spinup case with the Ekman pumping increased from a maximum $w_1 = -0.5$ to $w_2 = -1.5$, while Fig. 6 is the opposite spindown case with the Ekman pumping decreased from $w_1 = -1.5$ to $w_2 = -0.5$. Therefore, the final state (only the part where the new steady state has been established, that is, the part across which the wave fronts f_F and x_F have passed) of the spindown shown in Figs. 6g–i can be taken as the initial state of the spinup in Fig. 5 and vice versa.

We first investigate the spinup in Fig. 5. Before the spinup at $t = 0^-$, the initial state is the steady thermocline under w_1, in which the lower layer is motionless in the shadow zone (Fig. 6g–i). The circulation immediately after the spinup $t = 0^+$ is shown in Figs. 5a–c, and should be compared with the corresponding initial state Figs. 6g–i, respectively. Figure 5a depicts the interface depth (solid lines) and the barotropic streamfunction (dashed lines with arrows). The wave fronts f_F, x_F, B_2, and B are denoted by dot-dashed lines. One sees that the wave fronts x_F, f_F, and B have not moved yet. The interface remains unchanged because baroclinic waves and advection have not developed. However, an enhanced new Sverdrup flow $v_B = fw_2$ has been established over the basin because barotropic waves have passed across the basin. This in-

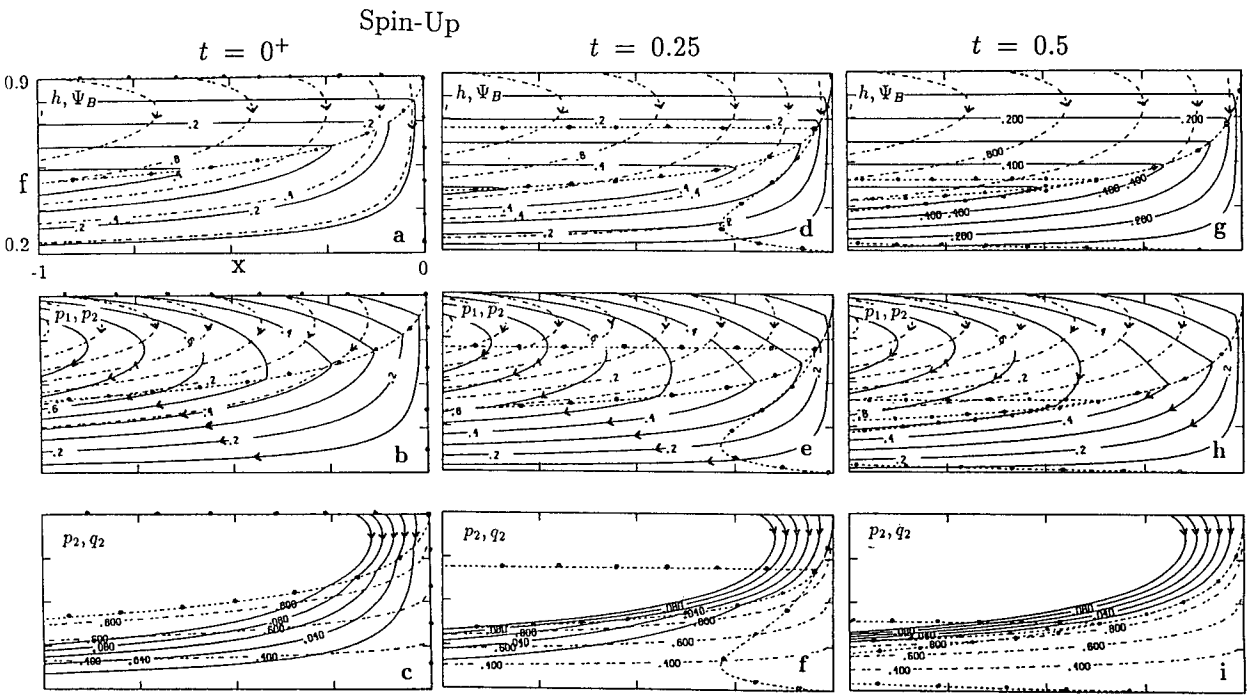

FIG. 5. Spinup from a maximum Ekman pumping $\max(w_1) = -0.5$ to $\max(w_2) = -1.5$. The parabolic Ekman pumping in (4.7) is taken with other parameters as $f_0 = 0.9$, $f_s = 0.2$; $x_w = -1$. In all cases, the wave fronts x_F, f_F, B are labeled and represented by dot-dash lines. Panels (a), (b), and (c) show the time immediately after the spinup at $t = 0^+$. The barotropic adjustment has finished, while the baroclinic adjustment has not started. Panel (a) shows the upper-layer depth in solid lines (contour interval = 0.1) and the barotropic streamfunction in dashed lines (contour interval = 0.2). The direction of the anticyclonic barotropical flow is also indicated by arrows; (b) shows the upper-layer pressure (or streamfunction) in solid lines (contour interval = 0.1) and the lower-layer pressure in dashed lines (contour interval = 0.1). The anticyclonic gyres in both layers are seen from the flow direction indicated by arrows; (c) further depicts the lower-layer pressure (solid lines) below $p_2 = 0.1$ [which is the smallest dashed contour in (b)] with a finer contour interval of 0.2 than in (b), therefore showing the flow in the shadow zone more clearly. One sees clearly that the water in the initial shadow zone now starts to move southward. The lower-layer potential vorticity (contour interval = 0.2) is plotted by dashed lines. Panels (d), (e), and (f) are the same as (a), (b), and (c), respectively, but at a later time $t = 0.25$; (g), (h), and (i) are also the same as (a), (b), and (c) but at an even later time $t = 0.5$. Compared with (a), (b), and (c), one sees that at $t = 0.25$ and $t = 0.5$, the thermocline deepens in the original shadow zone; wave front f_F propagates to establish a new ventilated zone; wave front x_F propagate westward, stopping the flow in the lower layer to build a new shadow zone. At $t = 0.5$, the new ventilated thermocline has been established over the entire basin except for the southwestern corner.

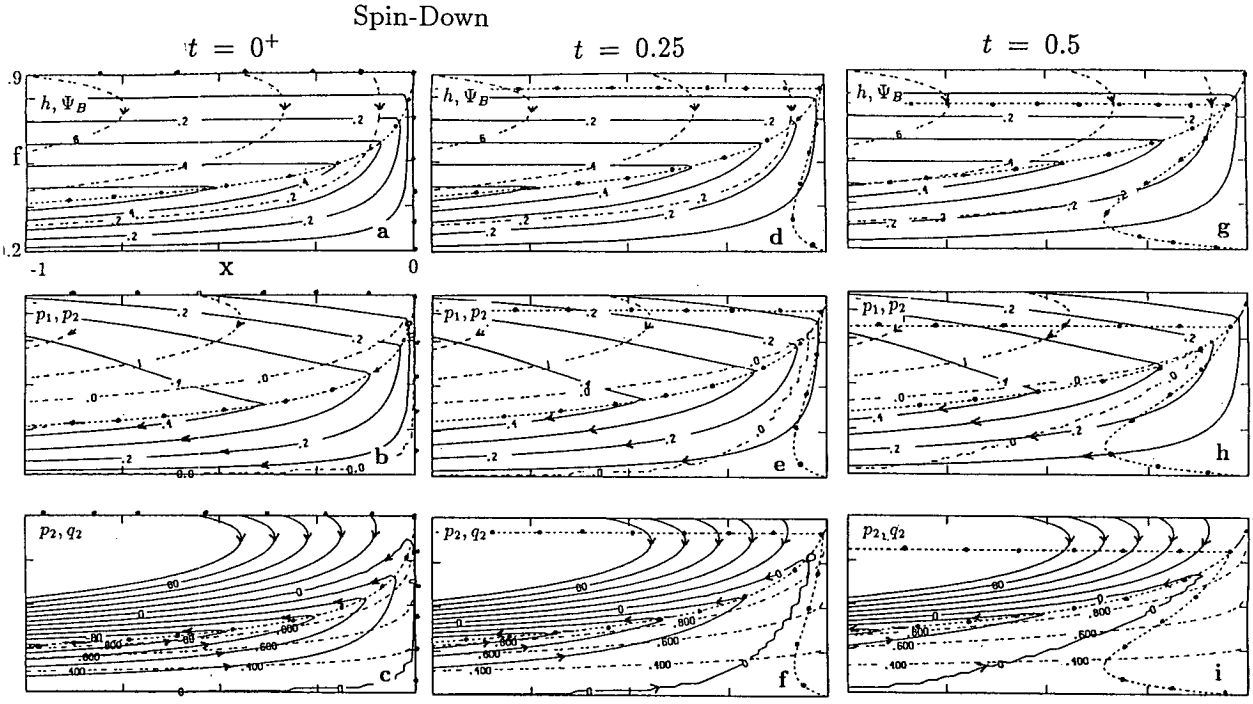

FIG. 6. As in Fig. 5 except for a spindown from a maximum Ekman pumping of −1.5 to a maximum pumping of −0.5. The most striking difference from the spinup case in Fig. 5 is that the interface now shallows in the original shadow zone, resulting in a northward flow in the lower-layer original shadow zone. As a result, the lower-layer fluid exhibits two counterrotating gyres: an anticyclonic gyre to the north and a cyclonic gyre to the the south. This can be seen clearly in (c). The northward flow and the cyclonic gyre in the original shadow zone reach the strongest after the spindown as shown in (c). Later, it decreases in both its strength and extent as shown in (f) and (i). The wave fronts x_F and f_F propagate much more slowly than in the spinup case in Fig. 5 mainly because of the much slower barotropic flow.

creased barotropic flow then intensifies the anticyclonic gyres in both layers. This is seen clearly in Fig. 5b, which shows the upper- and lower-layer pressures or streamlines in solid and dashed lines, respectively. It is interesting to see that, in the shadow zone, the lower-layer waters are no longer motionless. They start to move southward. The motion in the shadow zone can be seen more clearly in Fig. 5c, which shows a finer picture of the lower-layer flow in the shadow zone. These waters penetrate toward the potential vorticity $q_2 = f/(1 - h)$ isolines (dashed lines, Fig. 5c). The penetration implies a positive potential vorticity advection ($-\mathbf{v}_2 \cdot \nabla q_2 > 0$), which must produce a local increase of q_2, that is, a local deepening of the upper-layer thickness. Physically, with a spinup, the anomalous Ekman pumping is downward; that is, $\Delta w_e = w_2 - w_1 < 0$. After the barotropic adjustment, this downward Δw_e compresses the planetary vortex tube and produces an additional barotropic southward flow all over the basin. Therefore, the anticyclonic gyre is intensified in both layers. In particular, in the shadow zone where layer 2 waters were at rest before the spinup, waters now move southward.

The succeeding baroclinic developments are plotted in Figs. 5d–i. Figures 5d–f illustrate a later time $t = 0.25$. Compared with Fig. 5a, in Fig. 6d the upper layer has deepened, while the barotropic flow remains unchanged. The associated anticyclonic thermal wind intensifies the upper-layer flow and reduces the lower-layer flow (cf. Fig. 5e with Fig. 5b). There is always flow penetrating from the original ventilated zone to the original shadow zone, as shown more clearly in Fig. 5f as well as Fig. 5c. The flow tends to push old water in the original shadow zone farther southwestward and to replace part of this water. The eastern boundary wave front x_F radiates westward and catches the newly replaced water as well as the remaining water in the original shadow zone to establish a smaller, new shadow zone. On the other hand, the subduction front f_F advances southward. Accompanied by a stronger subducted flow caused by the stronger w_2, f_F builds up a larger new ventilated zone. The internal front B migrates slightly eastward to expand the original ventilated zone due to the increased Ekman pumping.

Figures 5g–i are for an even later time $t = 0.5$. The upper layer deepens farther in the original shadow zone (Fig. 5g). Wave fronts x_F and f_F continue to propagate to enlarge the new shadow zone and ventilated zone, respectively, at the expense of the original shadow zone and ventilated zone. The new ventilated thermocline is established over the gyre except for the southwestern corner. In the new shadow zone, the lower layer is again

at rest. If the time is long enough, one can imagine that the new ventilated thermocline will be established over the entire gyre.

We now turn to the opposite spindown process in Fig. 6. Before the spindown ($t = 0^-$), the initial state is similar to the final state of the previous spinup in Figs. 5g–i (except for the southwestern corner). After the spindown at $t = 0^+$ (Figs. 6a–c), compared with the initial stage in Figs. 5g–i, the interface remains unchanged; but the anticyclonic barotropic circulation (Fig. 6a), and the anticyclonic gyres in both layers (Fig. 6b) are reduced. Surprisingly, a cyclonic gyre emerges in the southern part, which includes a northward branch of flow in the original shadow zone and a southwestward return flow in the original ventilated zone (Fig. 6c). As a result, there are two counterrotating gyres in the lower layer, as seen clearly in Fig. 6c. The physics is the opposite to the spinup case. Now, the anomalous Ekman pumping is upward; that is, $\Delta w_e = w_2 - w_1 > 0$. Thus, stretching of the planetary vortex tube produces an additional barotropic northward flow, which tends to reduce the anticyclonic gyre. In the shadow zone where the water was previously motionless, the water now starts to move northward and therefore creates a cyclonic gyre.

In addition, the barotropic physics discussed above suggests that in the lower layer, the relative strength between the motion in the original ventilated zone and the original shadow zone is proportional to $v_{2ov}/v_{2os} \sim (w_2 - w_1)/w_2$. Since in a spinup $w_2 < w_1 < 0$, while in a spindown $0 > w_2 > w_1$, it follows that v_{2ov}/v_{2os} is larger in a spindown than in the opposite spinup. In other words, in a spindown, the two counterrotating gyres may be of comparable strength (once the spindown is not too weak), while in a spinup, the motion in the shadow zone is always weak compared with the ventilated zone. This feature can be observed by comparing Figs. 6b and 6c with Figs. 5b and 5c.

Figures 6d–i show the following baroclinic evolution. The interface shoals while the barotropic flow remains unchanged (Figs. 6d,g). The shoaling thermocline causes a weaker thermal wind, implying a weakening upper-layer flow (Figs. 6e,h). The front x_F advances westward and expands the new shadow zone. The extra waters for the expanded shadow zone mostly come from the western boundary inflow through the northward lower-layer flow in the south. The front f_F progresses slowly with a weaker subducted flow. The established new ventilated zone is smaller because the amount of subducted water is less than that going out to the western boundary. The much slower x_F and f_F (than that in Fig. 5) are primarily caused by the much reduced barotropic velocity. Now B moves slightly westward to increase the original shadow zone due to the weakened Ekman pumping. In the lower layer (see Figs. 6f,i), in contrast to the spinup, now there is always flow penetrating from the original shadow zone to the original ventilated zone, pushing waters northward. After entering the original ventilated zone, the waters turn back southwestward. This penetrated water accelerates the water exiting at the western boundary in the original ventilated zone.

In the limit of a complete spindown, $w_2 = 0$. After the fast barotropic adjustment, a cyclonic gyre fills out the whole basin to compensate the anticyclonic mass transport in the upper layer, resulting in a zero Sverdrup flow. Then, during the slow baroclinic evolution, the thermocline evolves as a giant purely baroclinic Rossby wave packet with the transports in each layer compensated. This packet propagates westward to induce the thermocline shoaling and deforms after meeting the western boundary.

It is interesting to see the resemblance between the flow pattern in the spindown case (Fig. 6) and that driven by a steady warm interface entrainment $w^* > 0$ (Luyten and Stommel 1986; Pedlosky 1986). Physically this is because in the spindown case, the interface shoaling produces an upward velocity (in the shadow zone, advection is usually less important, as seen later) just like an upward entrainment velocity. Therefore, there is a stretching on the planetary vorticity. Similarly, the flow pattern in a spinup process resembles that caused by cold entrainment.

d. Dynamic balances and mechanisms

According to the zones h_v, h_s, h_{ov}, h_{os}, as formed by characteristics, the dynamic balances in each zone are as follows. In a new ventilated zone, the subducted water produces a strong cold advection to balance the Ekman pumping deepening [$\mathbf{v}_B \cdot \nabla h = -(1 - h)w_e$]. In a new shadow zone, the eastern boundary Rossby wave balances the Ekman pumping [$C(h)h_x = -(1 - h)w_e$]. These two zones are analogous to the steady thermocline case [see (3.6) and (3.7)]. In an original ventilated zone, the rapidly varying cold advection dominantly balances the new Ekman pumping, leaving little variability [in the special case of (6.2), there is no variability], that is, $h_t = -\mathbf{v}_B \cdot \nabla h - (1 - h)w_e = 0$. In the original shadow zone, the dynamic balance is more complicated. Over most of the region, the density advection plays a secondary role. This can be observed in the upper panels of Fig. 5 and Fig. 6, where the barotropic flows are almost parallel to h in the original shadow zone. Nevertheless, in a spinup, there may be a strong warm advection in the southwestern corner of the basin. In contrast, in a spindown, the density advection is always negligible. In the limit of a complete spindown, $\mathbf{v}_B = 0$ and thus there is no density advection anywhere.[1]

[1] Under a general Ekman pumping, the sign of the advection is such that in a spinup, it is a cold advection (β spiral) in the northern and a warm advection (antiβ spiral) in the southern part of a subtropical gyre. Thus, in the south, the warm advection enhances the deepening due to the Ekman pumping; in the north, the cold advection

1) LOCAL DYNAMICS

So far, the dynamic balances are discussed according to zones formed by characteristics, whose sizes vary with characteristics. Hereafter, we study the local dynamics (i.e., at a fixed location). This approach will help us to gain a better insight into the dynamics from a more conventional viewpoint. Before going into further detail, we should realize that in the presence of a time-dependent Ekman pumping $w_e(t, x, f)$, an instantaneous ventilated zone and shadow zone will vary in size. Therefore, a ventilated zone at one time may be invaded by a shadow zone later and vice versa. Hence, unlike the case for steady Ekman pumping, it is no longer proper to divide an isopycnal only into a ventilated zone and a shadow zone. Now, it is proper to define the ventilated zone as the smallest instantaneous ventilated zone [under the weakest Ekman pumping $(w_e)_{\min}$], and to define the shadow zone as the smallest instantaneous shadow zone [under the strongest Ekman pumping $(w_e)_{\max}$]. This ventilated zone will not be invaded by any instantaneous shadow zone, and vice versa. Besides, there is a third buffer region, known as the alternative zone, between the ventilated zone and the shadow zone. The alternative zone is occupied by an instantaneous ventilated zone and shadow zone alternately. Denoting the shadow zone boundaries B under $(w_e)_{\max}$ and $(w_e)_{\min}$ as $B_{\max}$ and $B_{\min}$, respectively [see (3.3)], the above three zones can be expressed as *shadow zone:* $x_{B\max} < x$, *alternative zone:* $x_{B\min} < x < x_{B\max}$, and *ventilated zone:* $x < x_{B\min}$. Figure 7g displays schematically the three zones. The evolution of each term in (2.6a) is also plotted in Fig. 7 and will be examined as follows. The key for the evolution is that density advection changes rapidly (or barotropically) with the Ekman pumping, while the Rossby wave changes slowly (baroclinically).

2) THE LOCAL DYNAMICS IN THE SHADOW ZONE

An example of the shadow zone dynamics is shown in Figs. 7e,f in which the evolution of the four dynamic terms—the effective Ekman pumping, the Rossby wave, the density advection, and the vertical velocity at the interface—are depicted at the location x, $f = -0.5, 0.35$. These four quantities can be proven to be related by

$$w|_{z=-h} = -[h_t + \mathbf{v}_2 \cdot \nabla h] = -[h_t + \mathbf{v}_B \cdot \nabla h]$$
$$= Ch_x + (1 - h)w_e. \qquad (6.6)$$

Figure 7e shows the spinup in Fig. 5 and Fig. 7f shows the spindown in Fig. 6. Thus, Figs. 7e and 7f can be thought of as a cycle with one spinup and one spindown. The arrival of each wave front is also marked on the top of the figures. Before the spinup, the weaker Ekman pumping is balanced by the Rossby wave from the eastern boundary to maintain the old steady shadow zone with no vertical velocity at the interface (as shown in the final time of Fig. 7f). After spinup, the Ekman pumping is suddenly increased while the baroclinic process (the Rossby wave) has not developed yet. The excess Ekman pumping then forces a downward vertical velocity barotropically (through the barotropical divergence field), which in turn compresses the planetary vortex tube to force the originally motionless lower layer to flow southward. This location is now in the original shadow zone where the downward velocity starts to deepen the upper layer. This deepening suppresses the effective Ekman pumping, but causes an increase of the Rossby wave effect (both h and h_x increase). Therefore, the difference between the two mechanisms decreases monotonically. Equation (6.6) then means that the vertical velocity is reduced and that the lower-layer southward flow and the local deepening are reduced as well. This baroclinic process continues until the difference between the Ekman pumping and Rossby wave vanishes at about $t \approx 0.3$, which is the time when the newly excited eastern boundary Rossby wave (x_F) just reaches this location. Accordingly, the vertical velocity vanishes and a steady state is achieved. Afterwards, the eastern boundary Rossby wave begins to balance the Ekman pumping to maintain the new shadow zone. The warm advection develops to about one-third of the vertical velocity at about $t \approx 0.2$, contributing a significant part of the vertical velocity. Later, it decays with time because of eastern boundary waves.

The above steady shadow zone continues until the spindown occurs in Fig. 7f. A sudden decrease of the Ekman pumping takes place barotropically but the Rossby wave term has not changed yet. Therefore, the excess Rossby wave term begins to produce an upward velocity at the interface, which forces a northward flow in the lower layer. Since the advection is initially zero, this upward velocity mostly consists of a local shoaling. This location is once again in the original shadow zone. The subsequent baroclinic process is opposite to the spinup above. The shoaling increases the effective Ekman pumping, but decreases the Rossby wave effect and causes a weakening baroclinic thermal wind. At about $t \approx 0.7$, a new balance is reached between both mechanisms when the Rossby waves generated along the eastern boundary due to the spindown have just reached this point. Later, these waves balance the Ekman pumping and thus sustain the new steady shadow zone. In contrast to the spinup, the advection is a cold advection and remains weak.

3) THE LOCAL DYNAMICS IN THE VENTILATED ZONE

Figures 7a,b give an example in the ventilated zone at the point $(x, f) = (-0.5, 0.85)$. The dynamics differs

cancels part of the Ekman pumping deepening. The opposite occurs during a spindown, that is, there is cold advection in the southern part and warm advection in the northern part. A detailed discussion is not presented here.

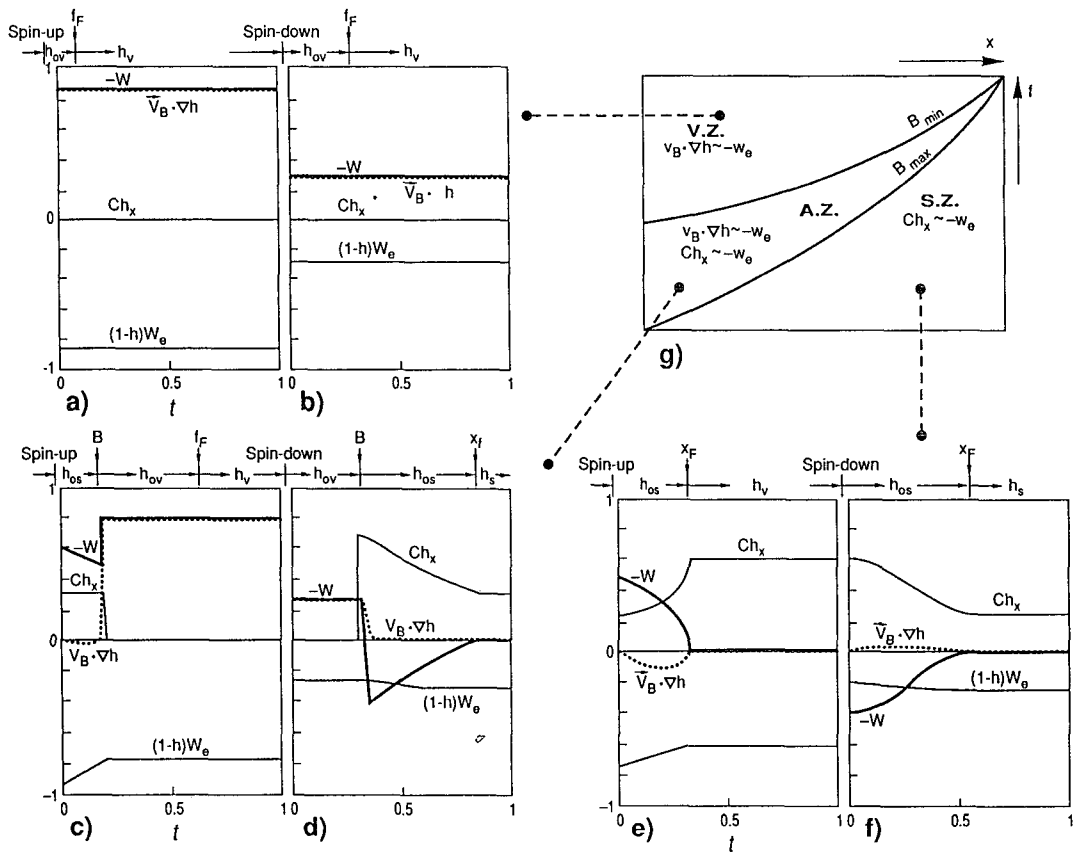

FIG. 7. The local evolution of each dynamical term (Ekman pumping, advection, and Rossby wave) in different regions. The vertical velocity is also plotted. The difference between the vertical velocity and the advection term is the local variability of the interface. The relation of each term is shown in Eq. (6.6). The spinup is from Fig. 5 and the spindown from Fig. 6. The arrival of each wave front is also marked by arrows on the top of each figure. (a) Spinup at $(x, f) = (-0.5, 0.85)$ (in the ventilated zone); (b) the same as (a) except with a spindown. In the ventilated zone, at all the times, the dynamical balance is between the cold advection and the local Ekman pumping. This balance adjusts immediately after the change of the Ekman pumping because of the barotropic adjustment. (c) Spinup at $(x, f) = (-0.5, 0.5)$ (in the alternative zone); (d) same as (c) but for a spindown. The Ekman pumping is balanced alternatively by the cold advection and Rossby wave. (e) Spinup at $(x, f) = (-0.5, -0.35)$ (shadow zone); (f) same as (e) except a spindown. Differing dramatically from the ventilated zone case in (a) and (b), in the shadow zone, one sees that the Ekman pumping is mainly dominated by Rossby waves. After the sudden change of Ekman pumping, the balance between the Rossby wave and the Ekman pumping is not reached after a finite time, which is the time for baroclinic adjustment. (g) A schematic figure showing different zones for local dynamics and the major dynamics balances in each zone in the case of a varying Ekman pumping: *V.Z* is the area of the minimum ventilated zone, *S.Z.* is the area of the minimum area of the shadow zone, and *A.Z* is the alternative zone where the instantaneous ventilated zone and shadow zone alternately exist.

dramatically from that in the shadow zone. Before the spinup, the cold advection balances the Ekman pumping to maintain the old ventilated zone. A strong downward velocity forces a southward motion in the lower layer. However, there is no local variability because the downward velocity solely consists of the advection $w(-h) = -\mathbf{v}_2 \cdot \nabla h$ [see (6.6)]. In other words, the warm vertical advection balances the cold horizontal advection. After the spinup, the position is in an original ventilated zone. Both Ekman pumping and cold advection endure a barotropic response and thus are increased linearly by the same amount. Consequently, a new balance is reached without any local baroclinic variability. In the present case with a flat bottom and a zonal profile, there is no baroclinic Rossby wave after the barotropic response. The wave front f_F from the outcrop line arrives at this location earlier than $t \approx 0.1$, which brings the newly subducted cold water. Later, a new ventilated zone is achieved between this new cold advection and the Ekman pumping. The spindown in Fig. 7b can be similarly discussed. It should be noted that for a more general case such as a tilted outcrop line, Rossby waves will appear. The original ventilated zone and the new ventilated zone will be different from each other. Therefore, there will be some baroclinic evolution. Nevertheless,

the advective nature of the ventilated zone seems to suggest that the dominant balance is still between the cold advection and the Ekman pumping.

Similar analysis applies to the alternative zone, but is not presented here (see Figs. 7c,d). Now, the internal wave front B can abruptly shut off the Rossby wave or the advection when B passes through one location. One can find that the alternative zone is controlled by the advection and Rossby wave alternately. Both the thermocline and circulation vary dramatically. Nevertheless, the size of the alternative zone is usually smaller than the other two (see the region where B sweeps through in Fig. 5 and Fig. 6).

7. Summary and discussion

A two-layer planetary geostrophic model is used to investigate thermocline variability under a suddenly changing Ekman pumping. The model includes a two-dimensional mean flow and thermocline structure. The effect of ventilation and the associated advection is particularly emphasized in the ventilated zone. It is found that the dynamics differs substantially between a shadow zone and a ventilated zone. In the shadow zone, the Rossby wave is the dominant mechanism for balancing the deepening forced by local Ekman pumping. After a sudden change in the wind field, the Ekman pumping changes rapidly, but the baroclinic Rossby wave evolves at a much slower time scale (years to decades). This mismatch of response time scales produces an imbalance in forcings and, in turn, results in a strong thermocline variability. However, in the ventilated zone, the cold advection replaces the Rossby wave to become the major opposing mechanism to the Ekman pumping. After a sudden wind change, both the Ekman pumping and the cold advection vary rapidly at the time scale of barotropic Rossby waves (about one week) to achieve a new steady balance, leaving little thermocline variability.

In addition, the evolution of circulation differs dramatically between a spinup and a spindown. For example, with a change in the Ekman pumping field, the lower-layer fluid in the shadow zone is no longer motionless. After a spinup, the lower-layer water moves southward because of the compression of planetary vortex tubes by the downward anomalous Ekman pumping. The associated circulation is an anticyclonic gyre. In contrast, during a spindown, the water moves northward because of the stretching of planetary vortex tubes by upward anomalous Ekman pumping. The lower-layer circulation now consists of two counter-rotating gyres: an anticyclonic gyre to the north and a cyclonic gyre to the south. In another paper with periodic Ekman pumpings, this thermocline circulation evolution will also be seen, with the increasing and decreasing Ekman pumping seasons corresponding, respectively, to spinup and spindown (Liu 1993a).

We should point out some limits of the above theory and possible refinements for the future. First, the unchanging thermocline structure in the ventilated zone is caused by the zonal outcrop line and the flat bottom. The flat bottom model used here captures the essential feature of a ventilated thermocline by allowing fluid to subduct. However, to simulate the bottom of the main thermocline, which is neither rigid nor flat, this flat bottom is artificial. Therefore, one should be cautious about the evolution in the ventilated zone. Nevertheless, the dominant subduction physics in the ventilated zone seems to suggest that the conclusion obtained here may be qualitatively correct, even for more general cases. The simplest model eliminating the artificial flat bottom is a $2\frac{1}{2}$-layer model, which will be studied in the future.

The unchanged ventilated zone has not taken into account the surface buoyancy variability. In fact, it is shown (Liu and Pedlosky 1993) that the surface buoyancy variability may cause strong thermocline variability in the ventilated zone, but it only affects the shadow zone slightly. Therefore, in our two-layer model, we reach the important conclusion: variability in ventilated regions is due predominantly to surface buoyancy variations, while variability in shadow zones arises mainly from changes in the wind forcing. Indeed, this conclusion can be inferred simply from the steady thermocline solution (3.2) and (3.3) (if we note that the effect of a varying surface heat flux or surface temperature can be simulated by the outcrop line f_o). The thermocline structure in the ventilated zone is $h_v = 1 - f/f_o$, which is independent of Ekman pumping or is solely determined by the outcrop line. Therefore, after a change of Ekman pumping, one may speculate that the thermocline structure still remains the same; but after a varying surface temperature (or outcrop line) the solution will be altered significantly. The opposite occurs for the shadow zone solution $h_s = \sqrt{2f^2 w_1(f)x}$, which is independent of the outcrop line or is solely determined by the Ekman pumping. However, as the vertical resolution is increased, the conclusion may be modified. One can show that in a $2\frac{1}{2}$-layer model, the steady LPS solution in the ventilated zone (under a zonal outcrop line) will depend on the Ekman pumping although the shadow zone is still independent of the outcrop line. In a $3\frac{1}{3}$-layer model (Luyten et al. 1983), the shadow zone thermocline becomes dependent of the outcrop line. Furthermore, what happens to a continuously stratified model [such as that of Huang (1986)]? Obviously, much work is needed.

Finally, we discuss some relevance to observations and numerical modelings. Observations have indicated that the annual response in the northern part of the subtropical gyres in both the North Pacific and the North Atlantic is mainly barotropic, while in the southern part the response is mainly baroclinic (Gill and Niiler 1973). Later observations (Price and Magaard 1980, 1986; White and Saur 1983) found no signals and very weak signals of interannual baroclinic

Rossby waves in the northern part of the subtropical gyre in the North Pacific and the North Atlantic, respectively. In contrast, in the southern parts of the subtropical gyres in both oceans, clear baroclinic Rossby wave signals are identified at annual and interannual frequencies. These observations are consistent with the theory here. The thermocline in the northern part of a subtropical gyre is mainly occupied by a ventilated zone, where the advection from the subducted water tends to balance the local Ekman pumping. As a result, little baroclinic Rossby wave advection exists. On the contrary, the thermocline in the southern part of a subtropical gyre is mostly occupied by a shadow zone, where advection plays little role. Baroclinic Rossby waves and local Ekman pumping dominate the response. Consequently, baroclinic waves are strong. Therefore, the different dynamic balances between a ventilated zone and a shadow zone, as found here, may offer an explanation for the lack of baroclinic signals in the northern parts of subtropical gyres.

Some numerical modeling under annual forcing has shown seasonal reversal of deep thermocline flow in the southeastern North Pacific (Spall 1991, personal communication) that is closely related to shadow zone dynamics. This seems to be consistent with the results in this paper. The oscillation of flow can simply be produced by barotropic response of the ocean to the varying wind. It is hoped that this work will stimulate more numerical modeling work to investigate the time-dependent thermocline. Since it is unlikely to obtain a comprehensive observation of ocean circulation at interannual time scales in a rather long time, numerical modeling is the best way to bridge the reality and theory.

Acknowledgments. This work started when the author was working on his Ph.D. thesis in the joint program of MIT and the Woods Hole Oceanographic Institution. The author is greatly indebted to Dr. J. Pedlosky for his advice and encouragement as well as his patient reading of previous manuscripts. Discussions with Drs. G. Flierl, R. X. Huang, and C. Wunsch were very helpful. The author thanks D. Marshall for his useful suggestions and careful reading of the manuscript. The comments from two anonymous reviewers have helped to clarify the paper substantially. This work is partly supported by the Division of Atmospheric Research, National Science Foundation, and by a NOAA postdoctoral fellowship in climate change.

APPENDIX

The Evolution of the Original Shadow Zone

Here, we discuss in detail the evolution of the original shadow zone solution (6.4). In (6.4), we see that the only time dependency comes from the initial latitude (for characteristics) $\hat{f}_i(f, t)$. As time evolves, the characteristics that reach a latitude f will come from a more northern initial latitude because of the southward characteristic speed $df/ds = v_B < 0$. Thus, $\hat{f}_i$ increases with time or $\partial_t \hat{f}_i(f, t) > 0$. We will examine how the increase of $\hat{f}_i$ affects the shape of the parabola in (6.4) during a spinup or a spindown. First, in (6.4a), $\hat{f}_i$ increases and then I decreases with time. For simplicity, $w_1(f)$ and $w_2(f)$ are assumed to possess the same spatial structure and thus in (6.4c) δ = const. On the whole interface it follows that

$$w_2(\hat{f}_i)/w_1(\hat{f}_1) = w_2(f)/w_1(f) = W_2/W_1 = \text{const} \begin{cases} >1 & \text{for spinup} \\ <1 & \text{for spindown,} \end{cases} \quad \text{(A.1)}$$

where W_1 and W_2 represent the strength of Ekman pumpings.

In a spinup process, (6.4b,c) and (A.1) give $-\infty < \delta < 0$, $G < 0$, $h_0 > 0$, $x_0 < 0$ for all times $t > 0$. Thus, a parabola must have its nose pointing toward the east because $G > 0$. Besides, the nose (x_0, h_0) is above the shadow zone profile for $h_s(f, x_0)/h_0(f) = \sqrt{1 - I^2\delta^{-1}} > 1$. The h_{os} part of the parabola always bulges downward, as does the initial steady state, and does not include its nose as drawn in Fig. 4a ($t = t_1$ profile). (The dashed line is drawn mainly for the illustration of the position of the nose and is not the physical part of the h_{os} solution.)

During a spindown, (6.4c) and (A.1) suggest $0 < \delta < 1$. As time evolves, in (6.4c), I starts from 1 to decrease. Initially, $I \approx 1$, thus $I^2 - \delta > 0$. Equations (6.4b,c) show that $x_0 > 0$, $h_0 < 0$, $G < 0$. The h_{os} part of the parabola bulges downward and does not include its nose as shown in Fig. 4b (the t_1 profile). Later, I may continue to decrease such that $I^2 - \delta = 0$ is reached at the transient time t_r satisfying

$$I^2[f, t_r(f)] - \delta \equiv 0. \quad \text{(A.2)}$$

Now, (6.4b) indicates that $G = \infty$ or the parabola degenerates to a straight line, which deepens westward as shown in Fig. 4b. Now, $I^2 - \delta$ changes sign to $I^2 - \delta < 0$. Equations (6.4b,c) indicate that both the curvature and nose change sign such that $G < 0$, $x_0 < 0$, $h_0 > 0$. Thus, the parabola should have its nose pointing toward the west. Since immediately after t_r, (6.4b) and (A.1) show that the nose is very deep and to the west (i.e., $x_0 \to -\infty$, $h_0 \to \infty$), the physical part of $h_{os}(<1 - f/f_o < 1)$ in (6.4a) does not include its nose. Therefore, a typical section during the transient stage is shown as the t_2 profile in Fig. 4b. Later, as $\hat{f}_i$ increases and I decreases further, the nose moves upward and eastward (or h_0 and $|x_0|$ is reduced). Eventually, it may occur that $x_0 = x_B$ and $h_0 = h_{ov}$ at the time t_b such that

$$x_0[f, t_b(f)] \equiv x_B[f, t_b(f)],$$
$$h_0[f, t_b(f)] \equiv h_{ov}[f, t_b(f)]. \quad \text{(A.3)}$$

(These two equations can be proven to occur simultaneously, so they give the same t_b.) Now, the nose is on the western edge of h_{os} (i.e., on B) and the interface is vertical there as shown in Fig. 4b. This is the marginal gravitational stability state and thus t_b is the first breaking time. After t_b, the h_{os} solution (6.4) becomes gravitationally unstable on its western side. Thus, on the western side, (6.4) is no longer a physical solution. The solution enters the breaking stage.

REFERENCES

Anderson, D. L. T., and A. E. Gill, 1975: Spin-up of a stratified ocean, with applications to upwelling. *Deep-Sea Res.*, **22,** 583–596.

——, and P. D. Killworth, 1979: Nonlinear propagation of long Rossby waves. *Deep-Sea Res.*, **26,** 1033–1050.

Cox, M. D., 1985: An eddy resolving numerical model of the ventilated thermocline. *J. Phys. Oceanogr.*, **15,** 1312–1324.

——, and K. Bryan, 1984: A numerical model of the ventilated thermocline. *J. Phys. Oceanogr.*, **14,** 674–687.

Dewar, W., 1987: Planetary shock wave. *J. Phys. Oceanogr.*, **17,** 470–482.

——, 1989: A theory of time-dependent thermocline. *J. Mar. Res.*, **47,** 1–31.

Gill, A. E., and P. P. Niiler, 1973: The theory of the seasonal variability in the ocean. *Deep-Sea Res.*, **20,** 141–177.

Huang, R. X., 1986: Solutions of the ideal fluid thermocline with continuous stratification. *J. Phys. Oceanogr.*, **16,** 39–59.

Keffer, T., 1985: The ventilation of the world's oceans: Maps of the potential vorticity field. *J. Phys. Oceanogr.*, **15,** 509–523.

Liu, Z., 1991: Time-dependent ventilated thermocline. Ph.D. thesis, Joint Program of MIT/Woods Hole Oceanographic Institution, 208 pp.

——, 1993a: Thermocline forced by varying Ekman pumping. Part II: Annual and decadal Ekman pumping. *J. Phys. Oceanogr.*, **23,** 2523–2540.

——, 1993b: Interannual planetary wave breaking in the presence of Ekman pumping and mean flows. *J. Fluid Mech.*, in press.

——, and J. Pedlosky, 1993: Thermocline forced by annual and decadal surface temperature variation. *J. Phys. Oceanogr.*, **23,** in press.

——, ——, D. Marshall, T. Warncke, 1993: On the feedback of the Rhines-Young pool on the ventilated thermocline. *J. Phys. Oceanogr.*, **23,** 1592–1596.

Luyten, J., and H. Stommel, 1986: Gyres driven by combined wind and buoyancy flux. *J. Phys. Oceanogr.*, **16,** 1551–1560.

——, J. Pedlosky, and H. Stommel, 1983: The ventilated thermocline. *J. Phys. Oceanogr.*, **13,** 292–309.

Pedlosky, J., 1983: Eastern boundary ventilation and the structure of the thermocline. *J. Phys. Oceanogr.*, **13,** 2038–2044.

——, 1986: The buoyancy and wind-driven ventilated thermocline. *J. Phys. Oceanogr.*, **16,** 1077–1087.

Price, J. M., 1986: Interannual baroclinic Rossby waves in the midlatitude North Atlantic. *J. Phys. Oceanogr.*, **16,** 2061–2070.

——, and L. Magaard, 1980: Rossby wave analysis of the baroclinic potential energy in the upper 500 meters of the North Pacific. *J. Mar. Res.*, **38,** 249–264.

Qiu, B., and T. M. Joyce, 1992: Interannual variability in the mid- and low-latitude western North Pacific. *J. Phys. Oceanogr.*, **22,** 1062–1079.

Rhines, P. B., 1986: Vorticity dynamics of the oceanic general circulation. *Ann. Rev. Fluid Mech.*, **18,** 433–447.

——, and W. R. Young, 1981: A theory of the wind-driven circulation I. Mid-ocean gyres. *J. Mar. Res.*, **40**(Suppl.), 559–596.

Roemmich, D., and C. Wunsch, 1984: Apparent changes in the climate state of the deep North Atlantic Ocean. *Nature*, **307**(5950), 447–450.

Stommel, H., and F. Schott, 1977: The β-spiral and the determination of the absolute velocity field from oceanographic station data. *Deep-Sea Res.*, **24,** 325–329.

Tabara, B., B. Thomas, and D. Ramsden, 1986: Annual and interannual variability of steric sea level along line P in the northeast Pacific Ocean. *J. Phys. Oceanogr.*, **16,** 1378–1398.

Talley, L. D., 1988: Potential vorticity distribution in the North Pacific. *J. Phys. Oceanogr.*, **18,** 89–106.

——, and W. B. White, 1987: Estimates of time and space scales at 300 meters in the midlatitude North Pacific from the TRANSPAC XBT program. *J. Phys. Oceanogr.*, **17,** 2168–2188.

Veronis, G., and H. Stommel, 1956: The action of variable wind stress on a stratified ocean. *J. Mar. Res.*, **15,** 43–75.

White, W. B., and J. F. Saur, 1983: Sources of interannual baroclinic waves in the eastern subtropical North Pacific. *J. Phys. Oceanogr.*, **13,** 531–544.